Published in final edited form as:
Acad Radiol. 2007 February ; 14(2): 207–218.

Initial Clinical Experience with Microwave Breast Imaging in Women with Normal Mammography

Paul M. Meaney[*], **Margaret W. Fanning**[*], **Timothy Raynolds**[*], **Colleen J. Fox**[*], **Qianqian Fang**[*], **Christine A. Kogel**[+], **Steven P. Poplack**[+], and **Keith D. Paulsen**[*]

[*] *Thayer School of Engineering, Dartmouth College, Hanover, NH USA*

[+] *Dartmouth Hitchcock Medical Center, Lebanon, NH USA*

Abstract

We have developed a microwave tomography system for experimental breast imaging. In this paper we illustrate a strategy for optimizing the coupling liquid for the antenna array based on *in vivo* measurement data. We present representative phantom experiments to illustrate the imaging system's ability to recover accurate property distributions over the range of dielectric properties expected to be encountered clinically. To demonstrate clinical feasibility and assess the microwave properties of the normal breast *in vivo*, we summarize our initial experience with microwave breast exams of 43 women categorized as BIRADS 1. The clinical results show a high degree of bilateral symmetry in the whole breast average microwave properties. Focal assessments of microwave properties are associated with breast tissue composition evaluated through radiographic density categorization verified through MR image correlation in selected cases. Specifically, both whole breast average and local microwave properties increase with increasing radiographic density where the latter exhibits a more substantial rise. These findings support our hypothesis that water content variations in the breast play an influential role in dictating the overall dielectric property distributions and indicate that the microwave properties in the breast are more heterogeneous than previously believed based on *ex vivo* property measurements reported in the literature.

Keywords

breast imaging; microwave tomography; microwave breast properties

I. Introduction

In 2004 alone over 200,000 new cases of breast cancer were diagnosed in the U.S. with roughly 40,000 women dying from the disease making breast cancer the second largest cause of female cancer deaths in the U.S. [American Cancer Society 2004]. There have been numerous reports demonstrating that early detection is the single most significant predictor of long term survival [Joy et al. 2005; Tabar et al. 2003]; therefore, improvements in detection may help to reduce the high mortality rates that currently exist. Mammography is the front line screening modality, but its weaknesses in terms of sensitivity and specificity are well documented [Joy et al. 2005]. While MR and ultrasound are currently used primarily in a diagnostic setting, there is room for improvement in differential diagnosis as well.

Over the past decade there has been a steady increase in the interest in using microwave imaging as a way of detecting breast cancers. *Ex vivo* studies have indicated that there is significant contrast in the dielectric properties of normal and malignant breast tissue [Chaudhary et al. 1984; Joines et al. 1994; Duck 1990]. However, it is well known that the breast is a heterogeneous organ whose composition varies significantly depending on a variety of factors [Kumar et al. 2005]. For example, Woodard and White [1986] have shown that the mammary glands typically contain significantly more water than adipose tissue. Thus, fibroglandular breast tissue would be expected to have higher dielectric properties than fat but with properties that are still lower than high water content tissues. Further, studies have shown that the amount of fibroglandular tissue can vary widely from fattier breasts (with very little) to dense breast (with substantially larger proportions) suggesting that the baseline electrical properties of the normal breast may be highly variable [Wei et al. 2004].

Information on normal breast electrical properties is particularly relevant given the recent excitement over using microwave imaging for breast cancer detection. Generally, the techniques presently being pursued fall into two primary categories: radar and tomography. With respect to radar technology, the most advanced concepts appear to be ultra-wideband microwave imaging via space-time beamforming [Xu et al. 2005; Davis et al. 2005], confocal microwave imaging [Fear et al. 2002; Yun et al. 2005] and near field synthetic focusing [Benjamin et al. 2001]. Studies of microwave tomography also exist and include reports by Bolomey et al. [1982, 1983, 1985], Liewei et al. [2002], Souvorov et al. [2000], Bulyshev et al. [2001], Meaney et al. [2000, 2003], Ciocan et al. [2004], among others. Most of these efforts (either radar or tomography) are occurring at the prototyping stage where the goal has been to identify and optimize the important design considerations rather than report on the electrical characteristics of breast tissue per se.

The goal of this paper is to summarize our findings on the average properties we have found in the normal breast obtained from exams using a microwave tomography imaging approach [Meaney 2000]. The data extends and supercedes an earlier report [Poplack et al. 2004] on the microwave properties of the normal breast by expanding considerably the frequency range involved and the number of cases evaluated. Additionally, the coupling liquid deployed is better matched to the electrical impedance of the breast making the images more accurate than those analyzed from the earlier study. The results obtained are presented in four parts. First, we have studied the measured electric fields (especially the phase) when a breast is pendant in coupling fluid surrounding the imaging array. Second, results from phantom studies with varying properties similar to those encountered in our clinical breast imaging experiments are described. Third, reconstructed images of normal breasts from exams where the coupling liquid properties are more optimized with respect to electrical match are shown. Finally, we present several cases comparing microwave images with their corresponding MR exams. The results are important because they establish norms against which microwave images of women with breast abnormalities can be compared.

II. Methods

A. Imaging Procedure

All of the images presented in this paper were reconstructed from data acquired on either phantoms or human subjects using our clinical system located at Dartmouth Hitchcock Medical Center. The hardware installation and reconstruction algorithm have been described in detail elsewhere [Meaney et al. 1995, 2000, 2001, 2003; Paulsen et al. 1995, 1999; Li et al. 2004]. Algorithmically, we deployed our standard 2D Gauss-Newton routine with a Marquardt regularization which includes a variance stabilizing transformation (log transformation) [Meaney et al. 2006] and the associated phase unwrapping strategies reported in Fang et al. [2006]. For all image reconstructions, we utilized an electric field finite element mesh having

3903 nodes and 7588 triangular elements. The reconstruction parameter mesh contained 559 nodes (equal to the number of parameters reconstructed) and 1044 triangular elements. In each case, the amount of measurement data was 240 acquisitions (16 transmitters × 15 receivers per transmitter). The reconstruction time for each image was a total of 5 minutes for 20 iterations computed on a Compaq 833 MHz Alpha workstation. The system performance specifications are summarized in Table 2. Figure 1 shows a photograph of the clinical prototype, a schematic diagram of the illumination configuration and a sample set of amplitude and phase projection data from an exam of a woman with scattered breast density. The positive amplitude projection reflects the fact that there is less attenuation of the signal propagating through the breast than in the background coupling medium with no target (i.e. breast) in place. The maximum phase projection varies slightly depending on the illumination direction reflecting the fact that each projection provides an independent piece of data, but overall, the projections and their maxima are relatively similar. In general, the magnitude of the maximum phase projection increases with frequency, size of the breast and permittivity contrast between the background liquid and target. Over the course of several years, we have collected illumination data from the breasts of numerous women utilizing a variety of liquid bath compositions ranging from 0.9% saline to various mixtures of glycerin and water. The properties presented here, are provided in terms of relative (to the value in a vacuum) permittivity and conductivity. For simplicity, the word *relative* has been dropped in the text and figure presentations but is implied uniformly throughout the manuscript. The symbol, ε_r, is also used and refers to the relative permittivity as well.

B. Phantom Experiments

In these experiments, we imaged a set of cylindrical liquid phantoms positioned in the imaging array. The monopole antennas were configured on a 15 cm diameter circle and their height adjustable through computer control. In these results, we imaged the phantoms with the antennas located 5 cm below the liquid surface to minimize surface coupling effects (in the absence of a subject in place). The resulting 2D image has a 13.5 cm diameter circular field of view concentrically positioned within the antenna array. Figure 2 shows the thin-walled plastic containers suspended in the coupling bath from above the tank. The electrical properties chosen to represent the fatty (FT), scattered (SC), heterogeneously dense (HD) and extremely dense (ED) breast were extrapolated from the 600 MHz clinical permittivity results data presented in Poplack et al. [2004]. The conductivity values were allowed to vary depending on the glycerin:water mixture. The phantoms were not intended to mimic exactly what would be encountered in actual clinical situations; however, they offer a reasonable spectrum of property levels (covering the range of expected values) over which to evaluate system performance.

C. *In Vivo* Tissue Property Study

We recruited and imaged 43 women with negative (BI-RADS 1) mammography as part of a separate clinical trial evaluating the use of microwave imaging for tumor detection. The clinical methodology has been reported previously [Poplack et al. 2004]. In brief, subjects were recruited following routine screening mammography interpreted as negative (BI-RADS 1). The study radiologist reviewed each subject's screening mammogram to confirm normality and to assess breast density. The study radiologist's assessment of breast density was based on the percentage of dense tissue within the breast as defined by BI-RADS criteria [American College of Radiology 2003]. Subjects with a discrepant assessment of breast density (between the initial clinical interpreter and study radiologist) were evaluated by a third radiologist, who provided the final breast density assessment for study purposes. Table 1 shows the distribution of density and age for the subject population.

Figure 3 presents a flow diagram of the subject recruiting, data acquisition and image reconstruction process. Once a subject agrees to participate, information about the trial is

provided and a signed IRB-approved HIPPA-compliant informed consent form is obtained. Prior to examination, the microwave imaging system is prepared by selecting the liquid coupling bath and performing a calibration (roughly 35 minutes). The clinical study coordinator assists the subject with the positioning her breast in the imaging tank. The exam data acquisition is completely computer controlled under the observation of a microwave system operator located in the adjacent room. The exam data collection requires approximately 7 minutes per each breast. Once the exam is completed, the data is transferred the data to a secure server for preparation and image reconstruction.

During each of these breast exams, we used our optimized liquid coupling bath of 83:17 glycerin to water mixture which produced nominal dielectric properties of $\varepsilon_r = 17.9$ and $\sigma = 1.13$ S/m at 1300 MHz. Data was acquired at seven frequencies from 500 to 1700 MHz in 200 MHz increments and at seven vertical positions from the chest wall in 0.5 to 1.0 cm increments depending on breast size in AP (anterior-posterior) diameter. The imaging sessions (for both breasts) were generally concluded in less than 15 minutes. Two-dimensional images were reconstructed off-line using our variance stabilizing imaging algorithm. For each participant 2D images were recovered for seven anatomically coronal planes of each breast – a procedure that was repeated for the 900, 1100, 1300 and 1500 MHz data sets. All data was processed by the microwave team and prepared for clinical evaluation.

The images were processed by using a custom MATLAB graphical user interface (GUI) to identify manually regions of interest (ROI) on the image for which the software automatically computed the mean and standard deviation of the properties in the selected zone. For each image both an elevated property ROI and the entire breast cross section were evaluated. The properties reported here were derived from analysis confined to the first two imaging planes closest to the chest wall to minimize 3D effects associated with the near-nipple breast curvature. We compared the properties obtained between left and right breasts and examined correlations between the imaged properties and subject breast density and age.

D. Water Content and MR Comparison

We imaged two women with normal breasts using both the T2 weighted MR and the microwave systems. For alignment purposes, we placed vitamin E capsules as fiducials at various locations on the breast during the MR imaging to identify the corresponding planes during the microwave exam. After the MR imaging session, the vitamin E capsules were replaced by black ink markings which were visible during the microwave study. Because the image data was not collected simultaneously, and the fact that the breast was more buoyant in the liquid bath than in air, the image registration was approximate. The fiducials provided reasonable estimates of the microwave imaging planes to which the MR slices corresponded.

III. Results

In the first of the following sections, we describe efforts to identify an appropriate coupling liquid based on direct measurements of the electric fields from a cohort of women examined with several different liquid mixtures. The resulting coupling bath mixture was then utilized in the following phantom and in vivo imaging studies to assess the capability of our system to evaluate the electrical properties of the normal breast. Finally, two sets of MR and microwave breast exams were compared to assess the degree to which the microwave images could recover appropriate estimates of the dominant features in the heterogeneous distributions available from the MR images.

A. Background Liquid Selection

The maximum phase projection (MPP) at 900 MHz was determined from the raw data of 147 volunteer imaging exams (data collected from December 2000 to September 2003). These exams included imaging experiments performed with 0.9% saline ($\varepsilon_r = 77.0$, $\sigma = 1.75$), and 70:30 ($\varepsilon_r = 46.4$, $\sigma = 0.93$ S/m), 80:20 ($\varepsilon_r = 26.9$, $\sigma = 0.98$ S/m), and 87:13 ($\varepsilon_r = 23.4$, $\sigma = 0.91$ S/m) glycerin:water background solutions. Pure glycerin has low permittivity ($\varepsilon_r = 9.2$, $\sigma = 0.35$ S/m) and is very soluble in water ($\varepsilon_r = 79.3$, $\sigma = 0.17$ S/m), so it can be easily combined with water to create solutions with intermediate properties [Meaney et al. 2003].

The MPPs from these exams for the imaging array position closest to the chestwall for both breasts of women with a range of radiographic densities were plotted versus the background solution in Figure 4. Here, we have displayed the field phase projection because it is predominantly a function of the permittivity while the magnitude is more closely related to the conductivity of the medium. There is a wide range of MPP values even for each background solution. While these variations are partially due to differences in breast cross-sectional size, the variability because of differences in radiographic density is also a factor. Distinct bands are formed for each background solution/radiographic density combination. The MPPs for women classified as having fatty breasts generally had the greatest (negative) values, with those for scattered (SC), heterogeneously dense (HD) and extremely dense (ED) breasts decreasing progressively. In fact, the MPPs for the 87:13 background, straddle zero, indicating that the average properties for some breasts were probably lower than that of the background whereas others were greater. Given this nominal zero cross over point and allowing for some property dispersion between 600 and 900 MHz, these results are consistent with those previously reported over the span of densities and age [Poplack et al. 2004].

B. Phantom Results

The phantom experiments were designed to investigate the influence of microwave property variability with radiographic density in the normal breast [Poplack et al. 2004; Joy et al. 2005] on the detection and characterization of modest sized inclusions typical of screening abnormalities (For the screening population examined at Dartmouth Hitchcock Medical Center, the average size tumor at time of detection has been reported to be 1.6 cm diameter [Poplack et al. 2000]). Images were reconstructed at 1300 MHz using a 79% glycerin ($\varepsilon_r = 21$, $\sigma = 1.3$ S/m) background coupled to two sets of four 10 and 7.5 cm diameter breast phantoms, respectively. The phantom mixtures were comprised of (1) 97% glycerin ($\varepsilon_r = 8.9$, $\sigma = 0.47$ S/m), (2) 88% glycerin ($\varepsilon_r = 13$, $\sigma = 0.83$ S/m), (3) 84% glycerin ($\varepsilon_r = 16.4$, $\sigma = 1.05$ S/m), and (4) 80% glycerin ($\varepsilon_r = 20$, $\sigma = 1.2$ S/m) and were labeled (FT) fatty, (SC) scattered, (HD) heterogeneously dense, and (ED) extremely dense, respectively, to mimic properties we have found to be reflective of the overall breast composition for these radiographic categories [Poplack et al. 2004]. The particular phantom permittivity values were nominally chosen by extrapolating the 600 MHz *in vivo* values reported in [Poplack et al. 2004] up to 1300 MHz. The 10 and 7.5 cm diameter phantoms were imaged with a 2 and 1 cm diameter “tumor” inclusion located in the lower left quadrant, respectively. The tumor inclusion consisted of a 55% glycerin solution ($\varepsilon_r = 51$, $\sigma = 1.45$ S/m), having permittivity values reflective of the 900 MHz tumor properties reported in [Joines et al. 1994]. The contrasts in the phantoms used here range from (a) 1.05 to 2.3 in breast-to-background and 2.5 to 5.7 in inclusion-to-breast permittivity and from (b) 1.08 to 2.7 in breast-to-background and 1.2 to 3.1 in inclusion-to-breast conductivity which are representative of those observed in our clinical series of breast abnormalities except, perhaps, for the low end of the inclusion-to-breast permittivity contrast where ratios closer to 1.1 occur in some benign conditions in the higher breast density categories. While not an exhaustive study of the biological contrast resolution per se, these phantom experiments establish important benchmarks for assessing imaging performance in terms of contrast detection and characterization accuracies.

Figures 5a and b show 1300 MHz reconstructed images for the two sets of four breast phantoms with the 2 and 1 cm tumor-like inclusions. The outline of the breast phantom is readily discernable in all cases except the ED phantoms (where resolution of the boundary is diminished due to low contrast with the background ~1.05). As expected, the recovered bulk ε_r and σ values for the phantoms progress monotonically from a low value (~5–10 permittivity; 0.2–0.4 S/m conductivity) for the FT case to levels nearly equal to those of the background for the ED case. The 2 cm inclusion is quantitatively localized in terms of size, position and property value in both image pairs. Specifically, the peak values at the center of the recovered inclusions were ε_r = 32.1, 33.1, 39.4, and 39.1 and σ = 1.37, 1.58, 1.58, and 1.57 S/m for the FT, SC, HD, and ED cases. In the smaller phantom cases, the outline of the breast target is readily discernable with the recovered properties increasing monotonically from the FT to ED cases. The recovered inclusion properties were not as high as those for the 2 cm perturbations, but the localization of elevated properties were still readily detectable. The peak values at the center of the recovered inclusions in the 1 cm cases were ε_r = 23.9, 27.9, 31.4, and 36.0 and σ = 0.86, 1.01, 1.16, and 1.18 S/m for the FT, SC, HD, and ED cases.

C. *In Vivo* Normal Subject Study

The first analysis in this section examined the overall symmetry of the images between contralateral breasts. This information is regularly used by reading radiologists when assessing suspicious zones within either side [Kopans 1997]. Figure 6 shows a scatter plot of the average recovered breast tissue properties from the left and right breasts at 1300 MHz in the image plane closest to the chest wall for all subjects. The correlations are high for both permittivity and conductivity with associated coefficients of 0.990 and 0.961, respectively. The corresponding permittivity and conductivity correlation coefficients for 1100 MHz were 0.986 and 0.919 while those for 900 MHz were 0.976 and 0.940. In general, the lower frequency correlations were still high but not as high as those at 1300 MHz, which may be due to a more accurate recovery of the overall property distributions from the increased resolution at higher frequencies.

In the second analysis, we examined the average microwave properties in the breast relative to radiographic density. In addition, when there was a localized increase in either the permittivity or conductivity of at least 2 cm in size (see Figure 9) within the overall breast boundary of the higher density categories (i.e. HD and ED), an ROI was selected for analysis (referred to as the fibroglandular ROI, fROI). In the lower density categories (i.e. FT and SC) spatially similar ROIs were evaluated even when there was little or no evidence of localized property increases. Figures 7a and b show the group of mean permittivity and conductivity values (at 1300 MHz) within each radiographic density category for both the overall breast and the fROI's. In general, both quantities increase with radiographic density for both permittivity and conductivity. It is clear that the fROI values increase at a faster rate with density than the overall breast average (subsequent analysis, not shown, indicates the overall average increase can be attributed largely to the increase in the fROI). Further, the microwave properties of the *in vivo* fROIs for the denser breasts can be quite a bit higher than the nominal whole breast average. These results are consistent with what is known about (a) fibroglandular tissue content as a function of radiographic density, (b) the differences in water content between the adipose and fibroglandular tissues *in vivo* (also see water content images in Section II D), and (c) the influence of water content on tissue dielectric properties as discussed by Foster and Schepps [1980,1981].

The data processed for the same image sets at 900 and 1100 MHz exhibit similar trends and are not shown here. They generally reflect the differences that would be expected from typical tissue dispersion characteristics. For instance, the average fROI permittivity values for the HD breasts ranged from 20.9 at 900 MHz to 21.1 at 1300 MHz where we would expect minimal

variation in the properties over the small frequency range. Interestingly, the corresponding conductivity values increased modestly but proportionally more from 0.47 at 900 MHz to 0.61 at 1300 MHz.

Figures 8a and b show the 1300 MHz average fROI permittivities and conductivities as a function of subject age for the four different breast densities. For the SC and FT densities, there is no apparent trend with age with the trend lines having a slightly positive, but not statistically significant slope with age (permittivity p-values of 0.63 and 0.45 for FT and SC cases, respectively, and conductivity p-values of 0.51 and 0.48 for the FT and SC cases, respectively). There is a downward trend for the heterogeneously dense category as a function of age with associated permittivity and conductivity p-values of 0.17 and 0.21, respectively. In general, the fibroglandular tissue is known to atrophy and be progressively replaced by fatty tissue with age, especially after menopause [Kumar et al. 2005] whereas, the lower density breasts contain less glandular tissue at earlier ages and, therefore, experience less tissue replacement by fat at advanced years. Therefore, these findings might be expected. While these HD values do not meet the accepted threshold for significance (0.05), it should be remembered that this is a fairly small sample number and it is intriguing that the HD p-values are quite a bit lower than the associated values for both the ED and SC data sets.

D. MR Comparison Results

One of the most consistent features in our microwave images has been localized permittivity increases for women with elevated radiographic breast density. These regions appear primarily in the permittivity images but are sometimes present in the corresponding conductivity maps as well, usually to lesser extent. In this study, we have compared standard T2-weighted MR sequence images with those from our microwave system to determine whether the increased permittivity zones observed in the microwave images correspond to actual features (i.e. fibroglandular tissue) in the breast as determined from MR scans. We were able to image only 7 subjects with both the microwave system and MRI primarily due to cost and access limitations. The breasts of these women reflected a range of densities from fatty to heterogeneously dense. To summarize our experience, we chose to present the two cases with the most prominent anatomical features in the MR exams (e.g. distinct zones of fibroglandular tissue concentration that varied in composition between the imaging planes acquired). For reference, the remaining 5 cases were more homogeneous but also exhibited good correlation between the microwave and MR images. Figure 9 illustrates the recovered permittivity (top) and conductivity (bottom) images for seven anatomically coronal planes of the right breast of a woman with heterogeneous density. Plane 1 is closest to the chestwall with each subsequent image pair separated in 1 cm increments. Underneath each plane is the corresponding MR image slice. (The two image sets are only approximately coregistered as described in Section II.D). For this case study, there is a distinct region in the lower left quadrant of the MR images that predominantly contains fibroglandular tissue relative to the surrounding regions. It appears to correlate well with the corresponding permittivity images where there is a dominant permittivity increase in the lower left quadrant extending all the way to the nipple (at the last plane, the outline of the breast has virtually disappeared in the permittivity image except for this significant property increase). There is some corresponding property increase in the conductivity images as well, but it is not as pronounced.

A second set of images from another subject serves to reinforce these points. In this case, for the left breast images shown in Figure 10, the woman had scattered to fatty radiographic density. The microwave and MR images are displayed in a similar format Figure 10. The MR images show minimal fibroglandular structure in the planes closest to the chestwall and progressively increasing amounts of fibroglandular tissue in the lower right quadrant as the planes approach the nipple. The permittivity images are relatively homogeneous for the first

few slices near the chestwall and exhibit a gradual property increase from plane 4 to plane 7 in the appropriate locations. The conductivity images are largely homogeneous.

IV. Discussion

We have studied the behavior of electromagnetic field projections measured across the breast *in vivo* and have been able to optimize a suitable coupling liquid for our tomographic imaging system. The glycerin:water combinations can be tailored to the actual breast properties reasonably well. While the current 83:17 glycerin:water bath has been satisfactory for microwave breast imaging at lower frequencies (1300 MHz and below), we are already exploring the use of specific baths for the various radiographic density subsets at higher frequencies where the phase projections will naturally increase.

The phantom studies presented here for the series of layered experiments are more advanced than those typically reported in the literature. In general, most of the phantoms used for image reconstruction have been small circular or irregularly shaped homogeneous targets [Pastorino et al. 2000; Coarsi et al. 2000], although some recent results [Semenov et al. 2005] have been shown for high contrast layered phantom shapes. In that study, the reconstructed permittivity of the surrounding layer was recovered accurately but the inclusion contained some artifacts and the corresponding conductivity images were of much lower quality. Our experiments show that inclusions are recovered quite well over a range of property values, contrast levels, sizes and shapes of the layered breast phantom. These studies support the integrity and robustness of the imaging system in the setting of breast examination given that the images were formed without *a priori* information through an iterative algorithm initiated with the property values of the homogeneous background.

The normal breast imaging study reveals several important points. Our results are consistent with expectations with respect to contralateral similarity, tissue composition and age variations. In particular, we have shown that the overall microwave property averages are generally higher than those reported in various *ex vivo* tissue studies [Chaudhary et al. 1984; Joines et al. 1994], especially for denser breasts. The heterogeneity in the microwave property distribution within the breast is also significant especially as breast density increases. While breast heterogeneity in terms of tissue composition and radiographic density is well accepted within the radiology community, the degree to which microwave properties vary within the breast has not been fully appreciated previously and may have been underestimated in the past [Chaudhary et al. 1984; Joines et al. 1994].

The comparison of microwave images with MR data is also quite revealing. While the spatial registration between the two modalities was not exact in the cases presented, the correlation of microwave properties with the underlying MR structure is intriguing. Fibroglandular tissue has significantly higher water content than the surrounding adipose. This water content distribution maps directly to the permittivity via the established Maxwell-Fricke mixture laws [Fricke 1925]. Interestingly, the conductivity component does not exhibit these features to the same extent. Hydration of proteins in the fibroglandular tissue complicates the mixture relationship. As suggested in [Foster and Schepps 1980, 1981], the conductivity would not be expected to rise appreciably until the overall water content exceeds approximately 60% which is consistent with the fibroglandular zones for the images in Section III.D being visible primarily in the permittivity component of the microwave images.

Overall, these results illustrate that clinical microwave tomographic imaging of the breast is feasible and that the images appear to produce clinically relevant information on breast tissue composition. This bodes well for the future as we expand to higher operating frequencies, 3D imaging techniques, and, of course, into the imaging of women with breast abnormalities.

References

American Cancer Society. Breast cancer facts and figures 2003–2004. American Cancer Society; Atlanta, GA: 2004.

American College of Radiology (ACR). ACR Breast Imaging Reporting and Data System, Breast Imaging Atlas. 4. Reston, VA: American College of Radiology; 2003. ACR BI-RADS - Mammography.

Benjamin R, Craddock IJ, Hilton GS, Litobarski S, McCutcheon E, Nilavalan R, Crisp GN. Microwave detection of buried mines using non-contact, synthetic near-field focusing. IEE Proceedings - Radar, Sonar and Navigation 2001;148:233–240.

Bolomey J-C, Izadnegahdar A, Jofre L, Pichot C, Peronnet G, Solaimani M. Microwave Diffraction Tomography for Biomedical Applications. IEEE Transactions on Microwave Theory and Techniques 1982;82:1998 – 2000.

Bolomey J-C, Jofre L, Peronnet G. On the Possible Use of Microwave-Active Imaging for Remote Thermal Sensing. IEEE Transactions on Microwave Theory and Techniques 1983;83:777–781.

Bolomey, J-C.; Michel, Y. Process and means for rapid point by point survey of body scanning radiation field. US Patent #4,552,151. 1985.

Bulyshev AE, Semenov SY, Souvorov AE, Svenson RH, Nazarov AG, Sizov YE, Tatsis GP. Computational modeling of three-dimensional microwave tomography of breast cancer. IEEE Transactions on Biomedical Engineering 2001;48:1053–1056. [PubMed: 11534841]

Caorsi S, Massa A, Pastorino M. A computational technique based on a real-coded genetic algorithm for microwave imaging purposes. IEEE Transactions on Geoscience and Remote Sensing 2000;38:1697–1708.

Chaudhary SS, Mishra RK, Swarup A, Thomas JM. Dielectric properties of normal and malignant human breast tissues at radiowave and microwave frequencies. Indian Journal of Biochemistry and Biophysics 1984;21:76–79.

Ciocan R, Jiang H. Model-based microwave image reconstruction: simulations and experiments. Medical Physics 2004;31:3231–3241. [PubMed: 15651607]

Davis SK, Tandradinata H, Hagness SC, Van Veen BD. Ultrawideband microwave breast cancer detection: a detection-theoretic approach using the generalized likelihood ratio test. IEEE Transactions on Biomedical Engineering 2005;52:1237–1250. [PubMed: 16041987]

Duck, FA. Physical Properties of Tissue: A Comprehensive Reference Book. Academic Press; London: 1990.

Fang Q, Meaney PM, Paulsen KD. Multi-dimensional phase unwrapping: definition and properties. IEEE Transactions on Image processing. 2006(in press)

Fear EC, Li X, Hagness SC, Stuchly MA. Confocal microwave imaging for breast cancer detection: localization of tumors in three dimensions. IEEE Transactions on Biomedical Engineering 2002;49:812–822. [PubMed: 12148820]

Foster KR, Schepps JL. Dielectric properties of tumor and normal tissues at radio through microwave frequencies. J Micro Power 1981;16:107–119.

Fricke H. A mathematical treatment of the electrical conductivity and capacity of disperse systems ii. The capacity of a suspension of conducting spheroids surrounded by a non-conducting membrane for a current of low frequency. Phys Rev 1925;26:678–681.

Joines WT, Zhang Y, Li C, Jirtle RL. The measured electrical properties of normal and malignant human tissues from 50 to 900 MHz. Medical Physics 1994;21:547–50. [PubMed: 8058021]

Joy, JE.; Penhoet, EE.; Petitti, DB. Saving women's lives: strategies for improving breast cancer Detection and diagnosis. The National Academy Press; 2005.

Kopans, DB. Breast Imaging. 2. Lippincott: Williams & Wilkins; 1997.

Kumar, V.; Abbas, AK.; Fausto, N. Robbins and Cotran Pathologic Basis of Disease. 7. Elsevier Saunders; 2005. p. 1119-1154.

Li D, Meaney PM, Raynolds T, Pendergrass SA, Fanning MW, Paulsen KD. A parallel-detection microwave spectroscopy system for breast imaging. Review of Scientific Instruments 2004;75:2305–2313.

Liewei, S.; Nolte, LW.; Zhong, QZ.; Liu, QH. Performance analysis for Bayesian microwave imaging in decision aided breast tumor diagnosis. Proceedings of the 2002 IEEE International Symposium on Biomedical Imaging; 2002. p. 1039-1042.

Meaney PM, Paulsen KD, Ryan TP. Two-dimensional hybrid element image reconstruction for TM illumination. IEEE Trans Ant and Prop 1995;43:239–247.

Meaney PM, Fanning MW, Li D, Poplack SP, Paulsen KD. A clinical prototype for active microwave imaging of the breast. IEEE Trans Microwave Theory and Tech 2000;48:1841–1853.

Meaney PM, Paulsen KD, Pogue BW, Miga MI. Microwave image reconstruction utilizing log-magnitude and unwrapped phase to improve high-contrast object recovery. IEEE Trans Medical Imaging 2001;20:104–116.

Meaney PM, Pendergrass SA, Fanning MW, Li D, Paulsen KD. Importance of using a reduced contrast coupling medium in 2D microwave breast imaging. Journal of Electromagnetic Waves and Applications 2003;17:333–355.

Meaney PM, Fang Q, Demidenko E, Paulsen KD. Residual error analysis in applying a log transformation to the microwave parameter estimation problem. IEEE Transactions on Medical Imaging. 2006 (submitted)

Paulsen KD, Meaney PM, Moskowitz MJ, Sullivan JM Jr. A dual mesh scheme for finite element based reconstruction algorithms. IEEE Trans on Med Imag 1995;14:504–514.

Paulsen KD, Meaney PM. Compensation for nonactive array element effects in a microwave imaging system: part I – forward solution vs. measured data comparison. IEEE Trans on Med Imag 1999;18:496–507.

Pastorino M, Massa A, Caorsi S. A microwave inverse scattering technique for image reconstruction based on a genetic algorithm. IEEE Transactions on Instrumentation and Measurement 2000;49:573–578.

Poplack SP, Tosteson AN, Grove MR, Wells WA, Carney PA. Mammography in 53,803 Women from the New Hampshire Mammography Network. Radiology 2000;217:832–840. [PubMed: 11110951]

Poplack SP, Paulsen KD, Hartov A, Meaney P, Pogue B, Tosteson T, Grove M, Soho S, Wells W. Electromagnetic Breast Imaging – Normal Tissue Property Values. Radiology 2004;231:571–580. [PubMed: 15128998]

Schepps JL, Foster KR. The UHF and microwave dielectric properties of normal and tumour tissues: variation in dielectric properties with tissue water. Physics in Medicine and Biology 1980;25:1149–1159. [PubMed: 7208627]

Semenov SY, Bulyshev AE, Abubakar A, Posukh VG, Sizov YE, Souvorov AE, van den Berg PM, Williams TC. Microwave-tomographic imaging of the high dielectric-contrast objects using different image-reconstruction approaches. IEEE Transactions on Microwave Theory and Techniques 2005;53:2284–2294.

Souvorov AE, Bulyshev AE, Semenov SY, Svenson RH, Tatsis GP. Two-dimensional computer analysis of a microwave flat antenna array for breast cancer tomography. IEEE Transactions on Microwave Theory and Techniques 2000;48:1413–1415.

Tabar L, Yen MF, Vitak B, Chen HH, Smith RA, Duffy SW. Mammography service screening and mortality in breast cancer patients: 20-year follow-up before and after introduction of screening. Lancet 2003;361:1405–1410. [PubMed: 12727392]

Wei J, Chan H-P, Helvie MA, Roubidoux MA, Sahiner B, Hadjiiski LM, Zhou C, Paquerault S, Chenevert T, Goodsitt MM. Correlation between mammographic density and volumetric fibroglandular tissue estimated on breast MR images. Medical Physics 2004;31:933–942. [PubMed: 15125012]

Woodard HQ, White DR. The composition of body tissues. The British Journal of Radiology 1986;59:1209–1219. [PubMed: 3801800]

Xu L, Bond EJ, Van Veen BD, Hagness SC. An overview of ultra-wideband microwave imaging via space-time beamforming for early-stage breast-cancer detection. IEEE Antennas and Propagation Magazine 2005;47:19–34.

Yun X, Fear EC, Johnston RH. Compact antenna for radar-based breast cancer detection. IEEE Transactions on Antennas and Propagation 2005;53:2374–2380.

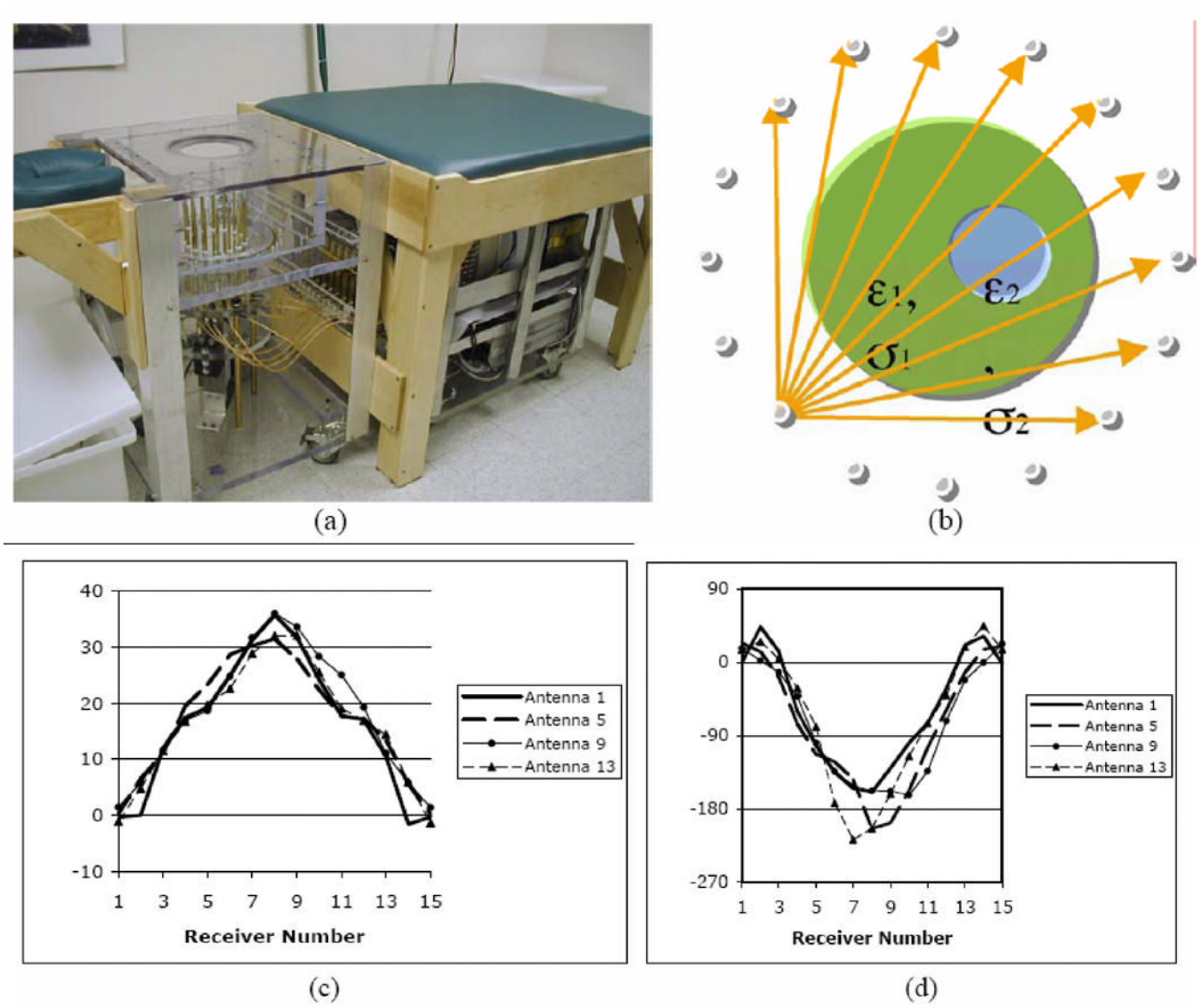

Figure 1.

(a) Photograph of the clinical microwave breast imaging prototype showing the illumination tank, exam platform and electronics cart (underneath bed); (b) 2D schematic diagram of the illumination and reception configuration; and representative (c) amplitude and (d) phase projections for a set of measured clinical data for a single imaging plane at 1300 MHz (data for only 4 of the 16 illuminations are shown).

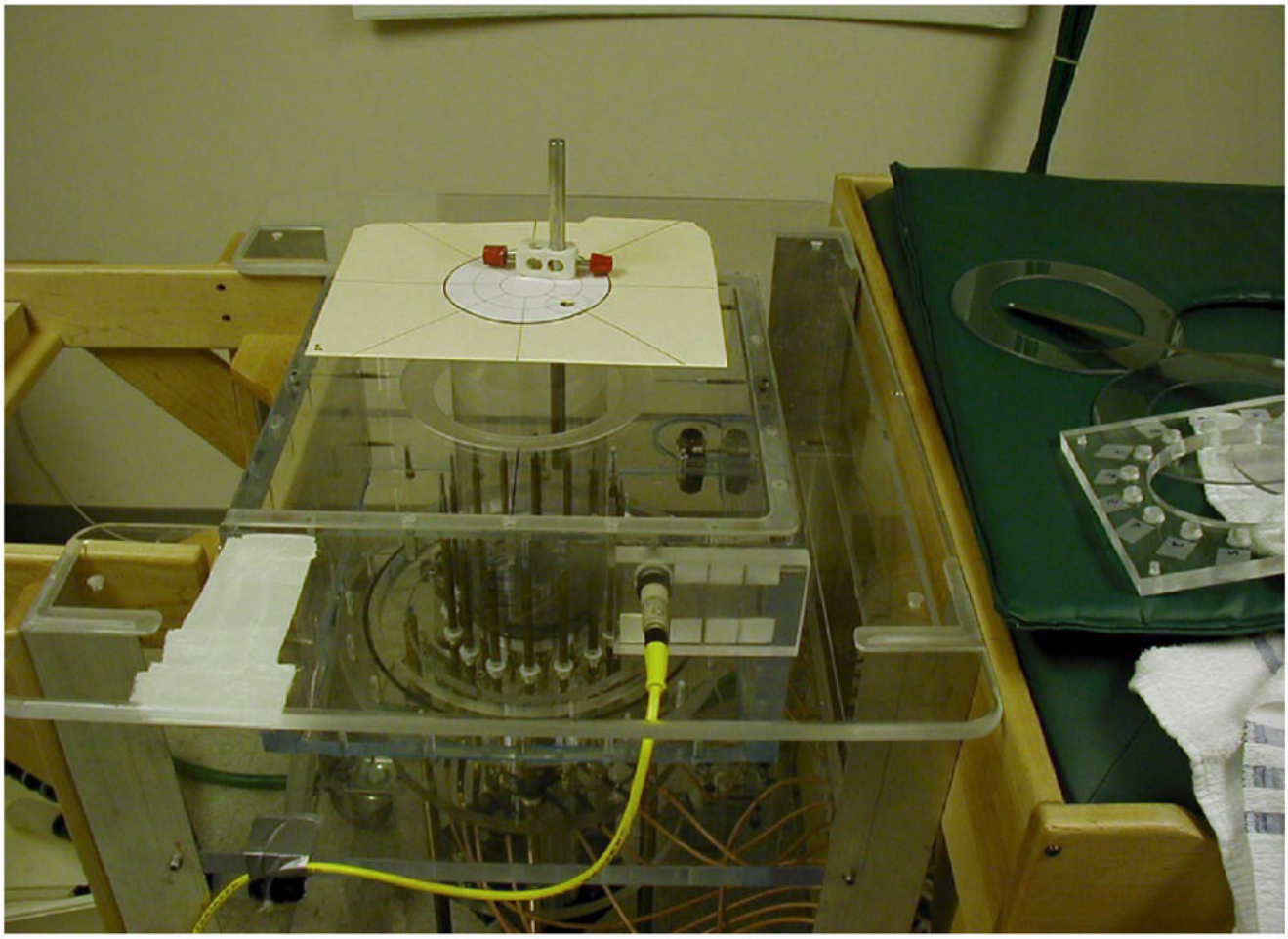

Figure 2.
Typical phantom experiment with liquid containers suspended from above the tank and integrated with an alignment fixture for accurate positioning.

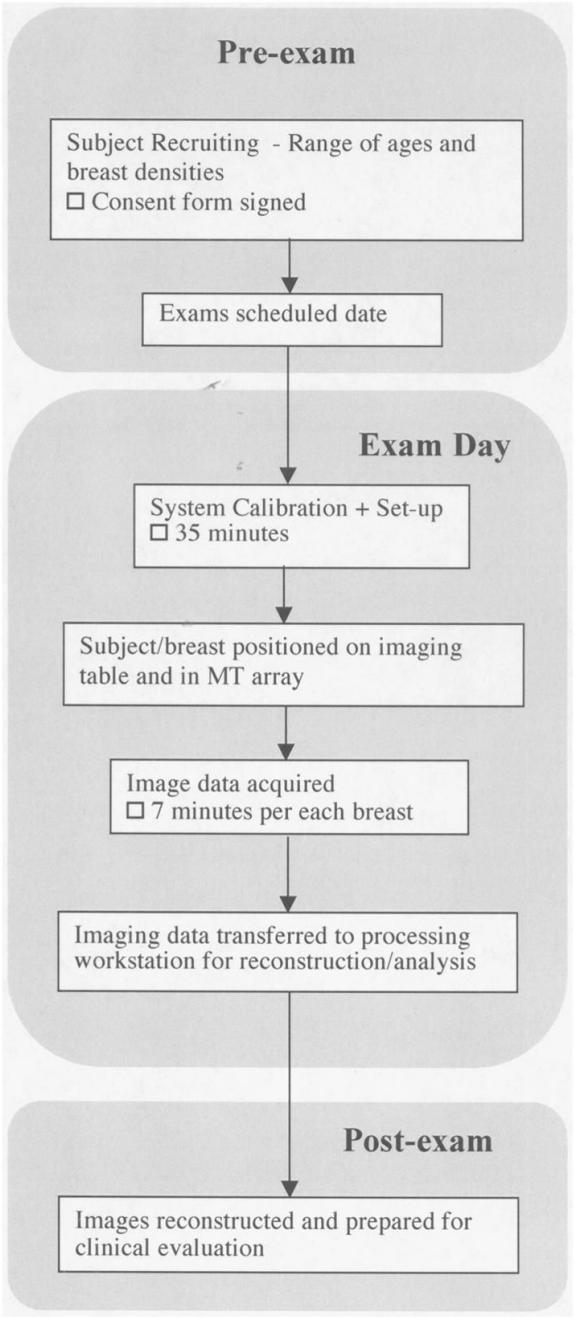

Figure 3.
Flow graph of the process followed for patient recruiting, examination and data processing.

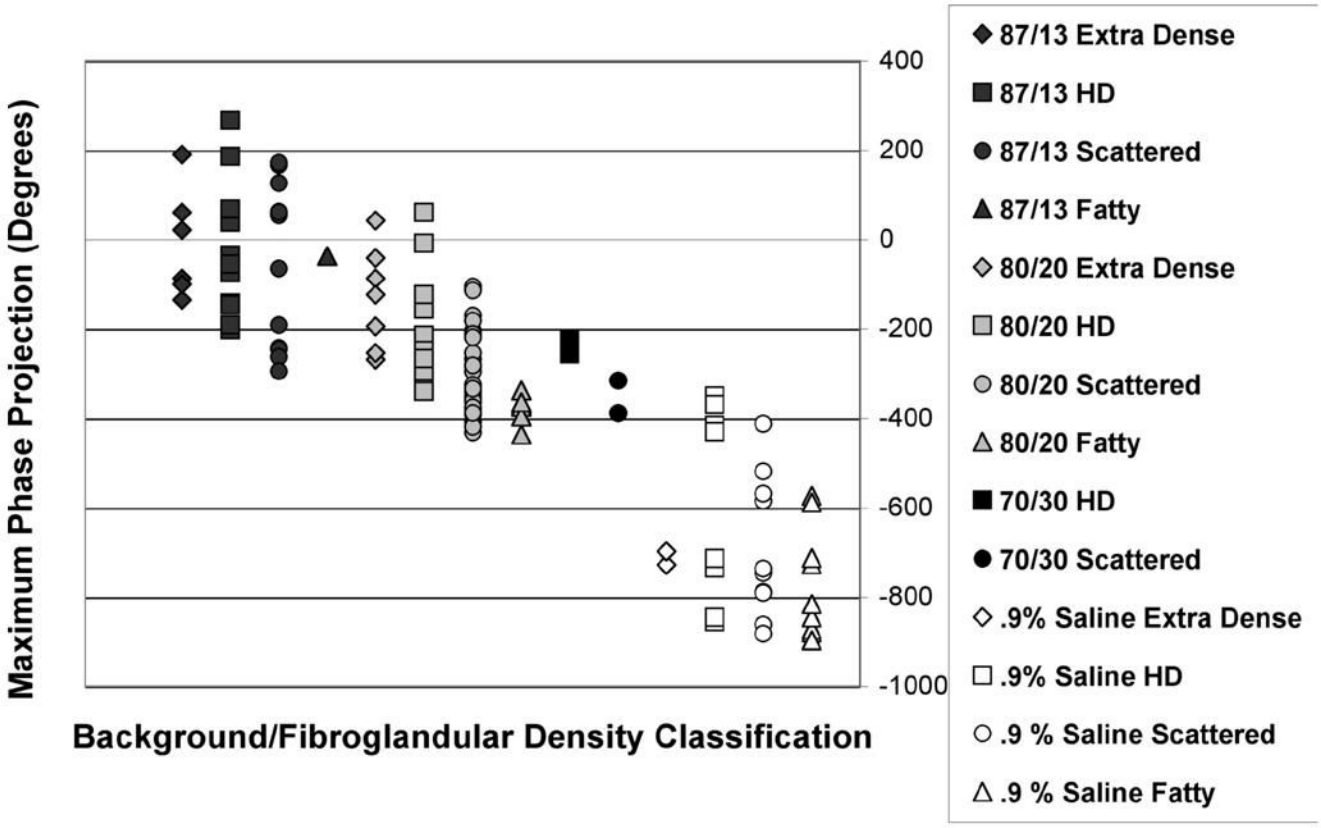

Figure 4.
Maximum phase projection data from 900 MHz imaging experiments of 147 volunteers utilizing several different coupling baths (0.9 % saline, and 70:30, 80:20, and 87:13 glycerin:water coupling baths) for women with a range of breast densities.

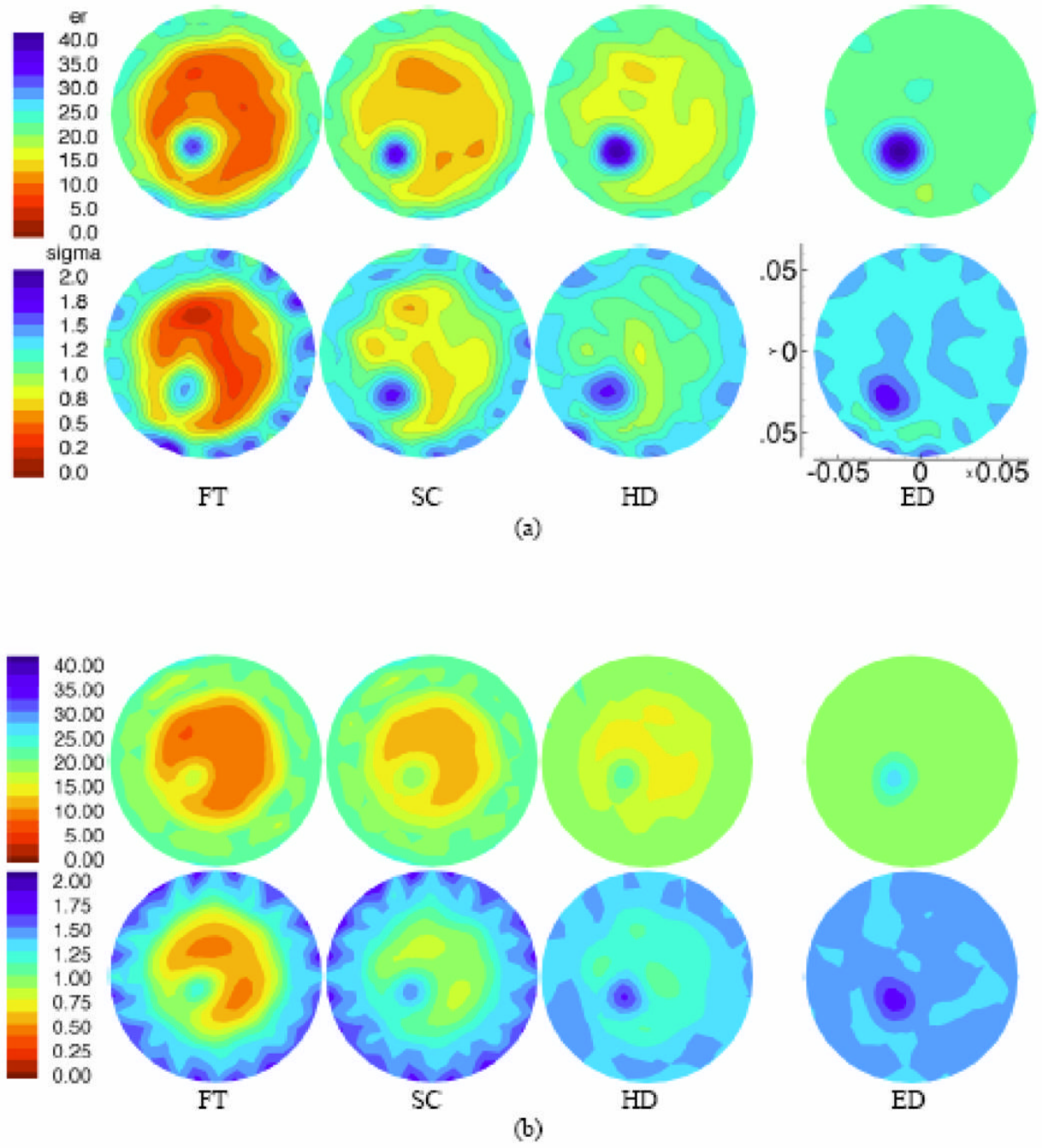

Figure 5.

1300 MHz permittivity (top) and conductivity (bottom) images for a (a) 10 cm phantom with a 2 cm inclusion, and a (b) 7.5 cm phantom with a 1 cm inclusion, respectively. Phantom designations (left to right): (FT) fatty, (SC) scattered, (HD) heterogeneously dense, and (ED) extremely dense have microwave properties which mimic those determined from *in vivo* images (see text for details). The imaging FOV is 13.5 cm in diameter in all cases and properties are reported on the common scales shown (left most image pair). Spatial dimensions are also the same in each case and a representative scale (in meters) is shown on the bottom right most image for the larger phantom case.

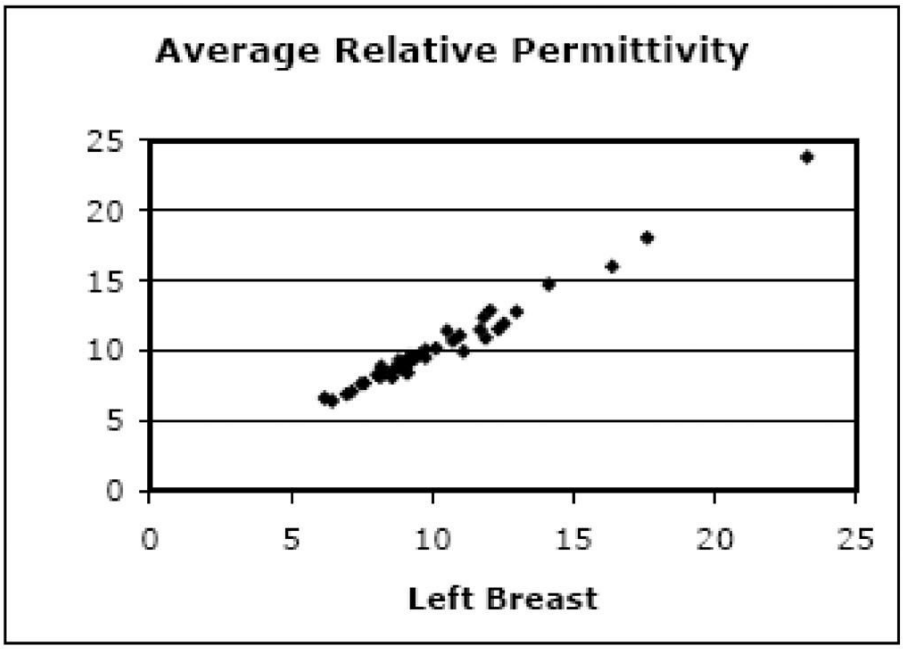

(a)

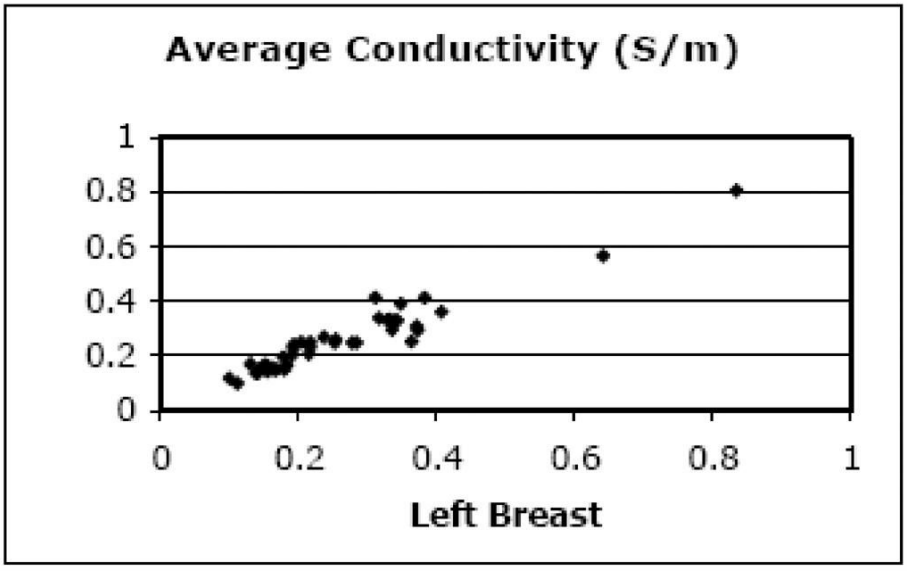

(b)

Figure 6.
Scatter plots of the 1300 MHz average (a) permittivity and (b) conductivity for the right versus left breasts of the 43 normal subjects.

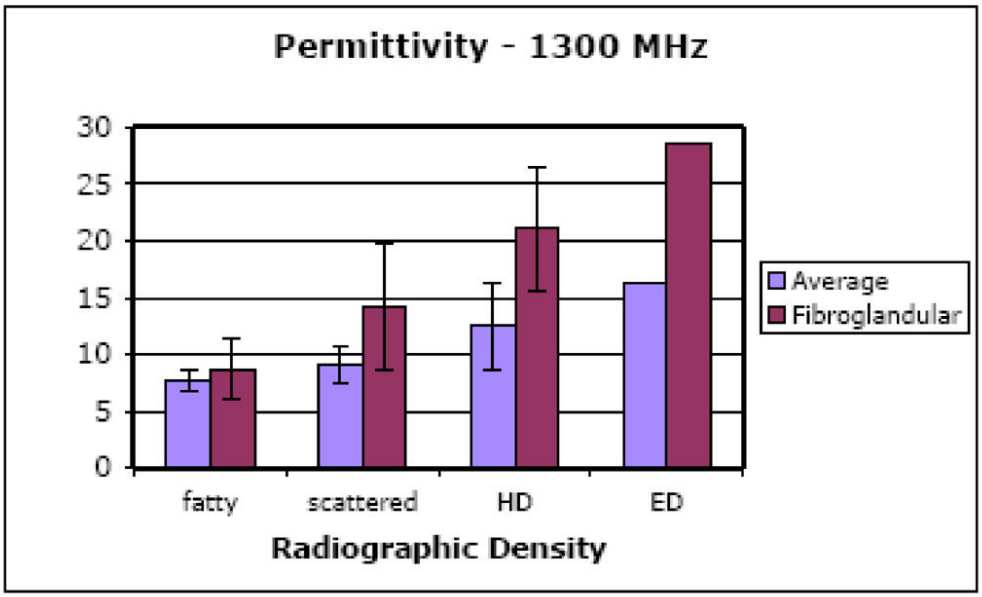

(a)

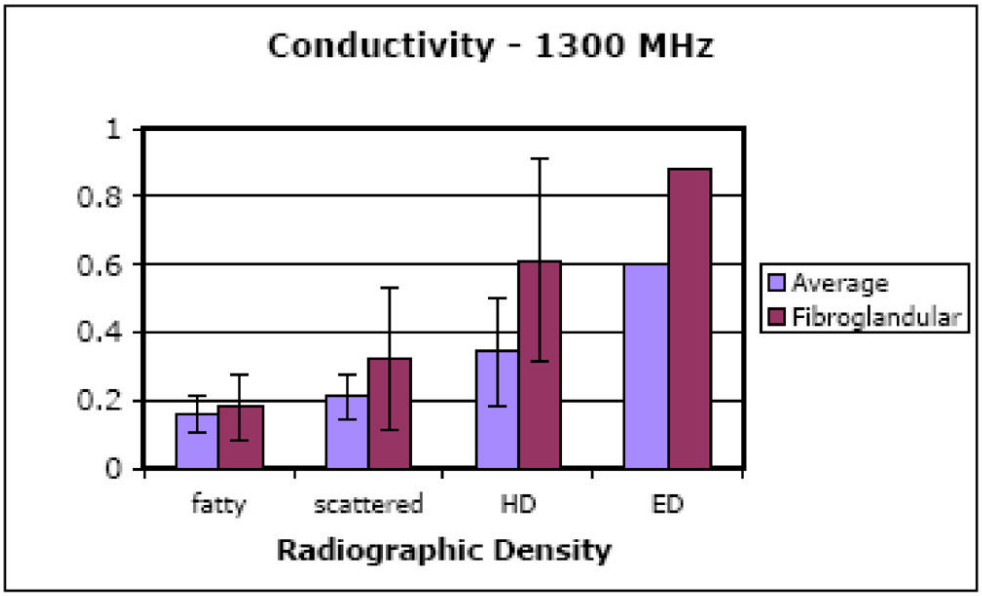

(b)

Figure 7.
Bar graphs of the 1300 MHz overall average and fibroglandular average (a) permittivity and (b) conductivity values as a function of breast density for the 43 normal subjects.

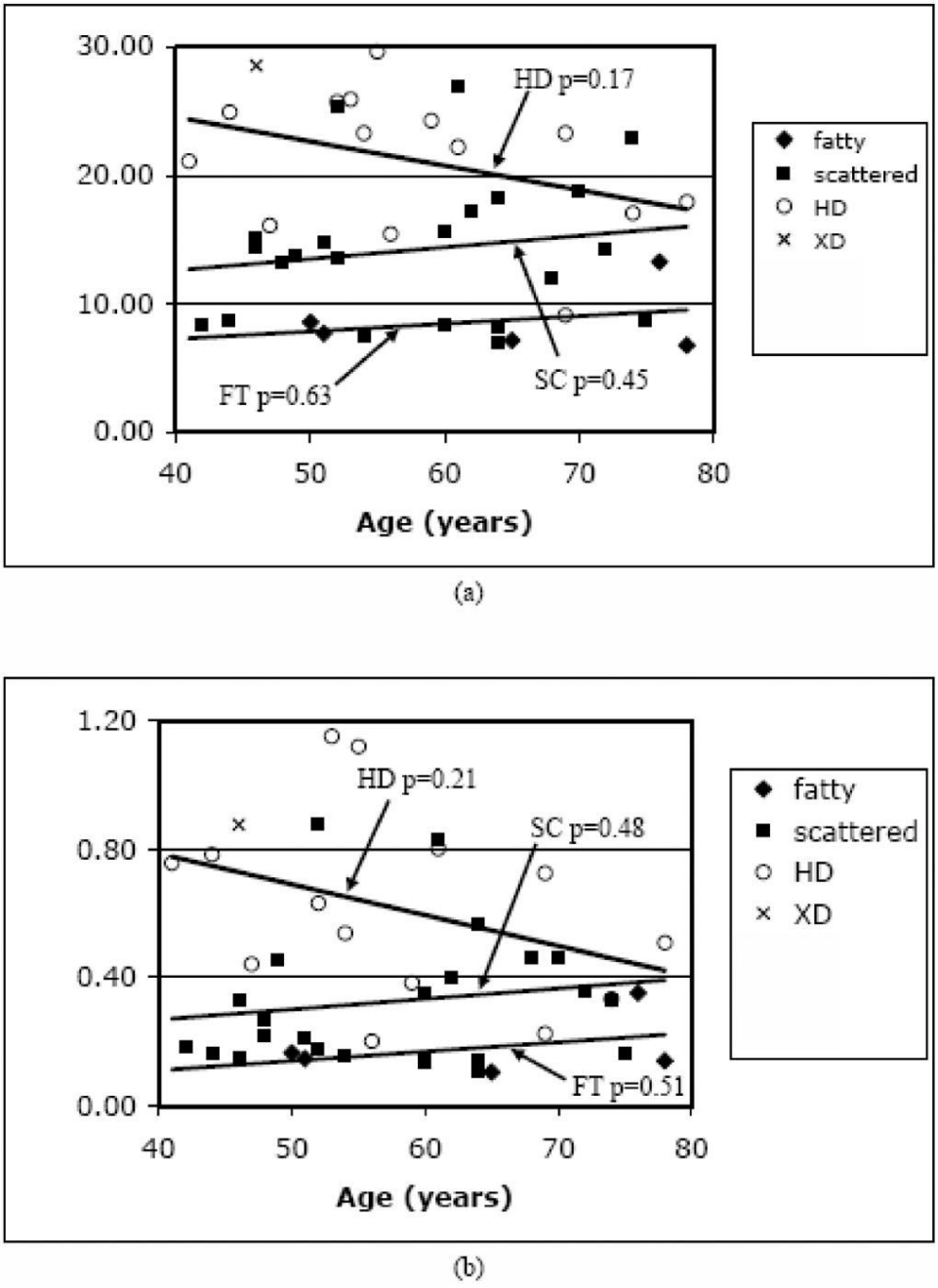

Figure 8.

Scatter plots of the 1300 MHz fibroglandular average (a) permittivity and (b) conductivity values grouped by radiographic density and graphed as a function of patient age. P-values for the trend lines are shown for each density category.

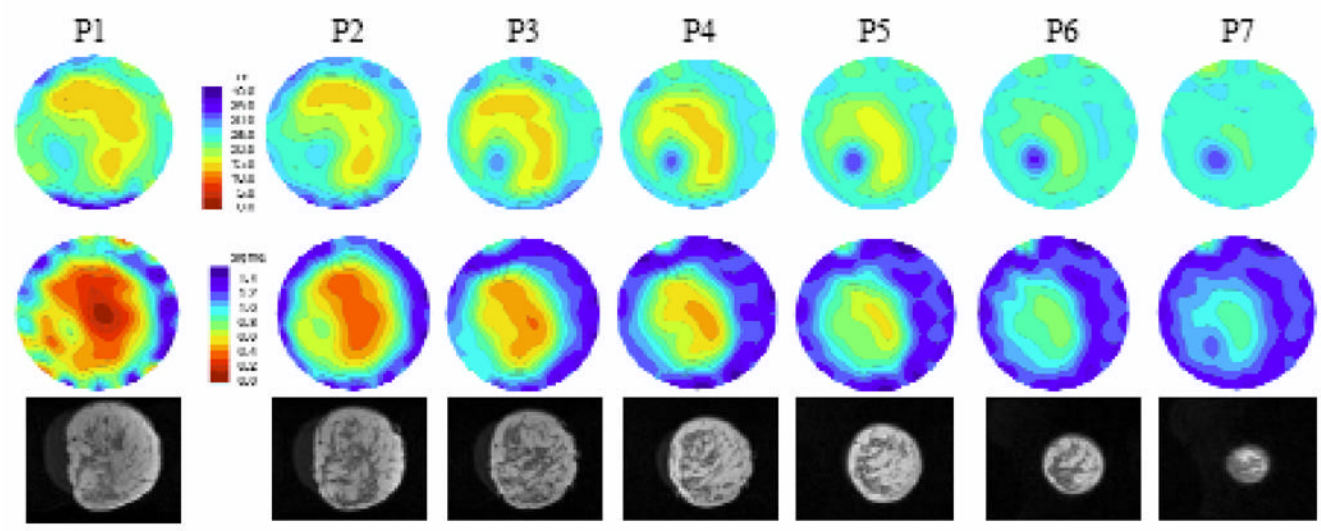

Figure 9.
Microwave (top row – permittivity and middle row – conductivity at 1100 MHz) and coregistered MR (bottom row) images in the same anatomically coronal view for the right breast of a woman with heterogeneously dense tissue. The labels (P1 to P7) above each image correspond to the plane of acquisition relative to the chestwall. The property and spatial scales are the same for all images. The microwave image FOV is fixed at 13.5 cm in diameter.

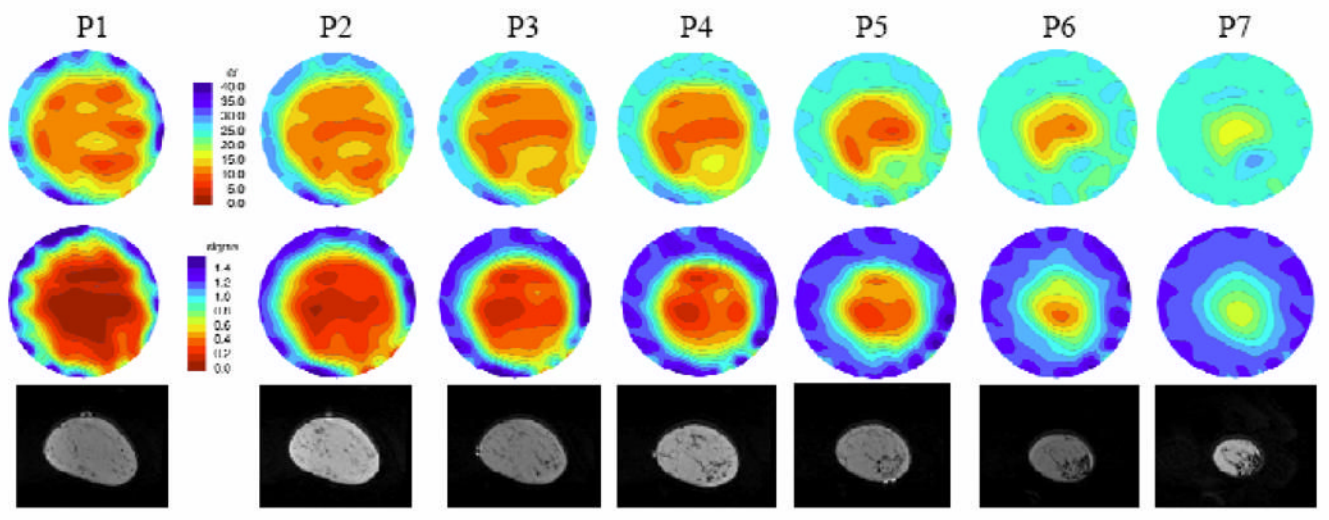

Figure 10.
Microwave (top row – permittivity and middle row – conductivity at 1100MHz) and coregistered MR (bottom row) images in the same anatomically coronal view for the left breast of a woman with fatty to scattered radiographic density. P1 though P7 (labels above each image column) indicate microwave tomograms spaced 1 cm apart beginning near the chestwall.

Table 1

Summary of the age and breast density distributions for the 43 women recruited for this imaging study.

Age	Density				Total
	Fatty	Scattered	Heterogeneously Dense	Extremely Dense	
40 – 49	0	7	3	1	11
50 – 59	2	4	6	0	12
60 – 69	1	8	3	0	12
70 –79	2	4	2	0	8
Total	5	23	14	1	43

Table 2

Summary of microwave tomography system performance specifications.

Performance Specifications	
Exam Geometry	Breast pendant in liquid bath
Imaging Planes	7
Coupling Bath	80:20 and 86:14 glycerin:water mixtures
Total Number of Images	49 (7 frequencies × 7 planes)
Exam Time	7 minutes
Frequencies	500 to 1700 MHz in 200 MHz increments
Power Transmitted	< 1 mW
Measurement Sensitivity	−130 dBm
Antenna Array	16 monopole antennas on a 15.2 cm diameter circle – non-contacting
Measurements/Image Set	240 (16 transmitters × 15 receivers per transmitter)
Image Properties	Electrical permittivity (ε_r) and conductivity (σ)
Reconstruction Time	< 5 minutes per image